

Direct-write patterning of nanoporous gold microstructures by in situ laser-assisted dealloying

JINGTING LI,¹ FUSHENG ZHAO,¹ AND WEI-CHUAN SHIH^{1,2,3,4,*}

¹Department of Electrical and Computer Engineering, University of Houston, 4800 Calhoun Rd. Houston, TX 77204, USA

²Department of Biomedical Engineering, University of Houston, 4800 Calhoun Rd. Houston, TX 77204, USA

³Department of Chemistry, University of Houston, 4800 Calhoun Rd. Houston, TX 77204, USA

⁴Program of Materials Science and Engineering, University of Houston, 4800 Calhoun Rd. Houston, TX 77204, USA

*wshih@uh.edu

Abstract: We report a novel patterning technique to direct-write microscale nanoporous gold (NPG) features by projecting laser patterns using a spatial light modulator (SLM) onto an Au/Ag alloy film immersed in diluted nitric acid solutions. Heat accumulation induced by the photothermal effect enables localized dealloying in such solutions, which is otherwise impotent at room temperature. Consequently, NPG micropatterns are formed at the irradiated spots while the surrounding alloy remains intact. We have studied the size of the patterned NPG microstructures with respect to laser power and irradiation time. The NPG microstructures become significantly more transparent compared to the original alloy film. The NPG microstructures also exhibit strong localized surface plasmon resonance (LSPR) which is otherwise weak in the original alloy film. Both the light transmission intensity and LSPR peak wavelength have been demonstrated to be sensitive to the local environmental refractive index as quantified by microscopy and spectroscopy.

© 2016 Optical Society of America

OCIS codes: (140.3390) Laser materials processing; (310.3840) Materials and process characterization; (160.4236) Nanomaterials.

References and links

1. L. Zhang, H. Chang, A. Hirata, H. Wu, Q. K. Xue, and M. Chen, "Nanoporous gold based optical sensor for sub-ppt detection of mercury ions," *ACS Nano* **7**(5), 4595–4600 (2013).
2. H. Qiu, L. Xue, G. Ji, G. Zhou, X. Huang, Y. Qu, and P. Gao, "Enzyme-modified nanoporous gold-based electrochemical biosensors," *Biosens. Bioelectron.* **24**(10), 3014–3018 (2009).
3. T. Fujita, P. Guan, K. McKenna, X. Lang, A. Hirata, L. Zhang, T. Tokunaga, S. Arai, Y. Yamamoto, N. Tanaka, Y. Ishikawa, N. Asao, Y. Yamamoto, J. Erlebacher, and M. Chen, "Atomic origins of the high catalytic activity of nanoporous gold," *Nat. Mater.* **11**(9), 775–780 (2012).
4. A. Wittstock, V. Zielasek, J. Biener, C. M. Friend, and M. Bäumer, "Nanoporous gold catalysts for selective gas-phase oxidative coupling of methanol at low temperature," *Science* **327**(5963), 319–322 (2010).
5. E. Seker, M. L. Reed, and M. R. Begley, "Nanoporous gold: fabrication, characterization, and applications," *Materials (Basel)* **2**(4), 2188–2215 (2009).
6. C. A. Chapman, S. Ly, L. Wang, E. Seker, and M. J. Matthews, "Utilizing dynamic laser speckle to probe nanoscale morphology evolution in nanoporous gold thin films," *Opt. Express* **24**(5), 5323–5333 (2016).
7. L. Zhang, X. Lang, A. Hirata, and M. Chen, "Wrinkled nanoporous gold films with ultrahigh surface-enhanced Raman scattering enhancement," *ACS Nano* **5**(6), 4407–4413 (2011).
8. Y. Jiao, J. D. Ryckman, P. N. Ciesielski, C. A. Escobar, G. K. Jennings, and S. M. Weiss, "Patterned nanoporous gold as an effective SERS template," *Nanotechnology* **22**(29), 295302 (2011).
9. F. Zhao, J. Zeng, M. M. Parvez Arnob, P. Sun, J. Qi, P. Motwani, M. Gheewala, C. H. Li, A. Paterson, U. Strych, B. Raja, R. C. Willson, J. C. Wolfe, T. R. Lee, and W. C. Shih, "Monolithic NPG nanoparticles with large surface area, tunable plasmonics, and high-density internal hot-spots," *Nanoscale* **6**(14), 8199–8207 (2014).
10. G. M. Santos, F. Zhao, J. Zeng, and W. C. Shih, "Characterization of nanoporous gold disks for photothermal light harvesting and light-gated molecular release," *Nanoscale* **6**(11), 5718–5724 (2014).

11. J. Zeng, F. Zhao, J. Qi, Y. Li, C.-H. Li, Y. Yao, T. R. Lee, and W.-C. Shih, "Internal and external morphology-dependent plasmonic resonance in monolithic nanoporous gold nanoparticles," *RSC Advances* **4**(69), 36682–36688 (2014).
12. M. M. Arnob, F. Zhao, J. Zeng, G. M. Santos, M. Li, and W. C. Shih, "Laser rapid thermal annealing enables tunable plasmonics in nanoporous gold nanoparticles," *Nanoscale* **6**(21), 12470–12475 (2014).
13. J. B. Zeng, F. S. Zhao, M. Li, C. H. Li, T. R. Lee, and W. C. Shih, "Morphological control and plasmonic tuning of nanoporous gold disks by surface modifications," *J. Mater. Chem. C Mater. Opt. Electron. Devices* **3**(2), 247–252 (2015).
14. G. M. Santos, F. Zhao, J. Zeng, M. Li, and W. C. Shih, "Label-free, zeptomole cancer biomarker detection by surface-enhanced fluorescence on nanoporous gold disk plasmonic nanoparticles," *J. Biophotonics* **8**(10), 855–863 (2015).
15. F. S. Zhao, J. B. Zeng, G. M. Santos, and W. C. Shih, "In situ patterning of hierarchical nanoporous gold structures by in-plane dealloying," *Mater. Sci. Eng. B* **194**, 34–40 (2015).
16. L. H. Qian and M. W. Chen, "Ultrafine nanoporous gold by low-temperature dealloying and kinetics of nanopore formation," *Appl. Phys. Lett.* **91**(8), 083105 (2007).
17. L. Y. Chen, J. S. Yu, T. Fujita, and M. W. Chen, "Nanoporous copper with tunable nanoporosity for SERS Applications," *Adv. Funct. Mater.* **19**(8), 1221–1226 (2009).
18. N. J. Jenness, R. T. Hill, A. Hucknall, A. Chilkoti, and R. L. Clark, "A versatile diffractive maskless lithography for single-shot and serial microfabrication," *Opt. Express* **18**(11), 11754–11762 (2010).
19. J. H. Slater, J. S. Miller, S. S. Yu, and J. L. West, "Fabrication of multifaceted micropatterned surfaces with laser scanning lithography," *Adv. Funct. Mater.* **21**(15), 2876–2888 (2011).
20. N. J. Jenness, K. D. Wulff, M. S. Johannes, M. J. Padgett, D. G. Cole, and R. L. Clark, "Three-dimensional parallel holographic micropatterning using a spatial light modulator," *Opt. Express* **16**(20), 15942–15948 (2008).
21. J. Qi, J. Li, and W. C. Shih, "High-speed hyperspectral Raman imaging for label-free compositional microanalysis," *Biomed. Opt. Express* **4**(11), 2376–2382 (2013).
22. J. Erlebacher, "An atomistic description of dealloying - Porosity evolution, the critical potential, and rate-limiting behavior," *J. Electrochem. Soc.* **151**(10), C614–C626 (2004).
23. X. Li, Q. Chen, I. McCue, J. Snyder, P. Crozier, J. Erlebacher, and K. Sieradzki, "Dealloying of noble-metal alloy nanoparticles," *Nano Lett.* **14**(5), 2569–2577 (2014).
24. J. Erlebacher, M. J. Aziz, A. Karma, N. Dimitrov, and K. Sieradzki, "Evolution of nanoporosity in dealloying," *Nature* **410**(6827), 450–453 (2001).
25. Y.-K. Chen-Wiegart, S. Wang, I. McNulty, and D. C. Dunand, "Effect of Ag–Au composition and acid concentration on dealloying front velocity and cracking during nanoporous gold formation," *Acta Mater.* **61**(15), 5561–5570 (2013).
26. J. Xu, Y. Wang, and Z. Zhang, "Potential and concentration dependent electrochemical dealloying of Al₂Au in sodium chloride solutions," *J. Phys. Chem. C* **116**(9), 5689–5699 (2012).
27. P. Loza, D. Kouznetsov, and R. Ortega, "Temperature distribution in a uniform medium heated by linear absorption of a Gaussian light beam," *Appl. Opt.* **33**(18), 3831–3836 (1994).
28. X. Y. Lang, L. H. Qian, P. F. Guan, J. Zi, and M. W. Chen, "Localized surface plasmon resonance of nanoporous gold," *Appl. Phys. Lett.* **98**(9), 093701 (2011).

1. Introduction

Porous materials are of great importance in many fundamental studies as well as technological applications. Among numerous porous materials, nanoporous gold (NPG) has attracted significant interest due to its unique properties such as high surface area to volume ratio, bi-continuous nanostructure, high electrical conductivity and thiol-gold surface chemistry. Potential applications can be found in biosensing [1, 2], catalysis [3, 4], and energy storage. NPG can be produced by dealloying of a gold alloy under open or applied electrochemical potential. Dealloying is a simple method where the less noble constituent of an alloy is selectively removed in a strong corrosive solution, e.g., concentrated nitric acid, while the more noble constituent forms an open porous network with bi-continuous pore and ligament structures. However, there is little control over the free corrosion process during dealloying. The desire to utilize NPG in various applications as well as fundamental studies motivates the development of novel fabrication and synthesis techniques since NPG properties are modified by morphological controls of the porous structures [5, 6].

Beyond the fabrication of semi-infinite NPG thin films, a few recent studies employed post-dealloying modifications to generate hierarchical NPG structures. L. Zhang *et al.* employed thermally induced wrinkling in NPG films to produce surface-enhanced Raman scattering (SERS) for molecular detection [7]. Y. Jiao *et al.* used direct mechanical impress to generate grating patterns with characteristic pitch of a few hundred of nanometers [8]. These

existing fabrication methods define the structural modulation after dealloying, thus can be classified as post-dealloying patterning. Our group recently developed a novel fabrication approach for sub-micron NPG disks by pre-dealloying lithographic patterning followed by dealloying [9]. The large surface area and hot-spots inside the nanoporous structures have contributed to an average SERS enhancement factor exceeding 10^8 and high photothermal conversion efficiency (>50%) [10]. In addition to size engineering, the plasmonic properties of NPG disks have been tuned by oven annealing [11], rapid laser photothermal annealing [12] and surface modifications [13]. NPG disk substrates have been employed for biomolecular sensing in a novel stamping approach, in microfluidic devices, and based on different detection mechanisms including surface-enhanced fluorescence and surface-enhanced near-infrared absorption [14]. More recently, we reported an *in situ* NPG micropatterning method by geometrical constraints to form hierarchical NPG structures during dealloying [15].

In this paper, we present another *in situ* NPG micropatterning method by localized laser heating, during which dealloying occurs at the laser focal spots due to elevated temperature. It is known that the dealloying rate increases with rising temperature and decreases with lowering acid concentration [16, 17]. Therefore, dealloying can occur at elevated temperature even in diluted acid which otherwise has negligible dealloying effects at room temperature. However, simply raising the temperature does not provide spatial selectivity to form NPG micropatterns unless the heating can be localized. Our solution is to employ laser-induced photothermal effect for localized heating. Using a spatial light modulator (SLM), nearly arbitrary micropatterns can be designed and fabricated. The non-contact nature of this technique is well suited for the processing of substrates immersed in an aqueous environment. Further, this technique shares the same advantages as maskless laser direct-writing which has found numerous applications [18, 19].

2. Methods and materials

The experimental setup consists of a 532 nm continuous wave (CW) laser (Spectra Physics Millennia Xs) with its beam expanded to ~ 7 mm in diameter. The expanded beam was incident on an SLM (Boulder Nonlinear XY Phase Series) which performs phase modulation and produces the desired pattern. The modulated beam was then fed through the back port of an inverted microscope (Olympus IX70) to irradiate the alloy sample. The full-width at half-maximum (FWHM) of a single laser spot was $1.5 \mu\text{m}$ on the sample with projecting precision error less than 200 nm. The holograms for phase modulation were pre-calculated and loaded into the SLM using Gerchberg-Saxton algorithm [20]. A camera (Thorlabs DCC1545M) was mounted at the front port of the microscope to record transmission bright-field images using a top tungsten halogen lamp. Alternatively, the transmitted light exited via the side port was directed toward a spectrograph (Acton 2300) and a charge-coupled device (CCD) detector (PIXIS 400BR). This system was originally built for parallel hyperspectral high-speed Raman microscopy [21], where more details can be found.

A typical sample was prepared by evaporating 5 nm Cr and 20 nm Au onto a glass substrate, followed by sputtering of a 90 nm thick $\text{Au}_{28}\text{Ag}_{72}$ (atomic percentage) alloy layer. The as-prepared samples were immersed in $20 \mu\text{L}$ 3.65M HNO_3 aqueous solution on a coverslip placed at the sample plane of the microscope where the projected laser pattern irradiated on the alloy film. After patterning, the samples were thoroughly rinsed with DI water and dried.

3. Results

The dealloying process can be described by the model of the concurrent dissolution of the less noble metal Ag and the diffusion of the more noble metal Au [22–24]. The steady-state dissolution rate can be described by $k_{dis} = \nu_{dis} \exp(-(nE_b - \phi) / k_B T)$, where ν_{dis} is a prefactor,

E_b is the total bond energy for an atom with n neighbors, and ϕ is the free corrosion potential. While Ag is being removed, the diffusion of Au atoms results in the formation of nanopores whose pore size as a function of time can be approximated by $d(t)^4 = KtD_s$, where diffusivity $D_s = D_0 \exp(-E_a/k_B T)$, E_a is the activation energy, and K and D_0 are constants [16]. The dealloying front velocity depends exponentially on the Au/Ag atomic ratio and acid concentration for a given temperature [25]. For a given alloy composition, the reaction rate is lowered by reducing the acid concentration [26], but can be increased at elevated temperature. The resulting pore distribution and pore size are therefore functions of temperature and time.

Temperature-dependent dealloying in diluted nitric acid

To establish the proof-of-concept of our approach, as prepared Au/Ag alloy films were immersed in 3.65M HNO₃ aqueous solution for 20 s at 9 different temperatures from room temperature (24 °C) to 99 °C. Scanning electron microscopy (SEM) images and pore size statistics are shown in Fig. 1. No dealloying was observed between 24 °C and 71 °C, so the SEM images for temperatures in between are not shown here. Sporadic pores started to appear at 78 °C, but lacks bi-continuity. As the temperature increased, it could be observed that the porosity increased and bi-continuous structures started to form. In the case of 20 s immersion, the initial temperature for dealloying is ~78 °C for our alloy composition and nitric acid concentration. For fully developed bi-continuous NPG structures, 99 °C was shown to be necessary.

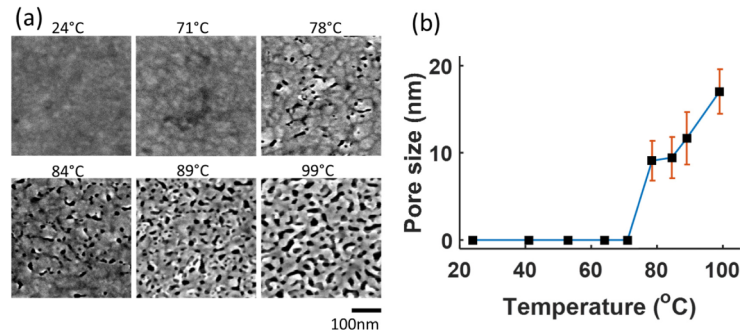


Fig. 1. (a) SEM images of dealloyed samples corresponding to 6 different temperatures. (b) Pore sizes after dealloying at different temperatures. Errorbars denote the standard deviation.

Laser direct-write patterning of NPG microstructures

When the laser was focused on the alloy thin film, a round spot NPG microstructure was formed. The spot generated by irradiation of 3.2 mW for 10 s is shown in the SEM image in Fig. 2(a). At the center of the spot, as shown in Fig. 2(b), the pore size is 21 ± 2 nm and the surface pore coverage is around 50%. The porous structure transitioned gradually from the center to the outer edge. The bright-field image [Fig. 2(c) inset] and its normalized cross-sectional intensity profile [Fig. 2(c)] show a distinct plateau over a $1.3 \mu\text{m}$ diameter with transmission intensity larger than 90% of the maximum intensity. The contour of this area is circled in Fig. 2(a), where the diameter of the NPG microstructure is defined as the width of the region with >90% intensity in light transmission. The pore size statistics from the NPG spot in Fig. 2(a) and a fitted Gaussian curve of mean $\mu = 0$ indicating the center and standard deviation $\sigma = 1.1$ are shown in Fig. 2(d), where random pore measurements are taken from each of 13 different radii from the center. Within the diameter threshold, the mean pore size ranges from 14 to 21 nm, while outside the diameter threshold, the mean pore size drops to the range from 5 to 11 nm. The light-transmission imaging was then used to evaluate *in situ*

dealloying results in future experiments. To show the transition of the NPG structure, SEM images taken at the center, inside the boundary, outside the boundary, and far away from the boundary of the NPG spots are shown in Fig. 2(e)-2(h), respectively. A gradual morphological evolution has been observed that the pore size and connectivity decrease while the ligament size and connectivity increased at a farther distance to the laser irradiation center.

Au/Ag alloy and NPG structures are known light absorbers and therefore photothermal heating is an effective mechanism to generate local heating. It is well known that dealloying cannot occur simply by photothermal effect at the power level in any of our experiments. Thus even though the exact temperature near the alloy-solution interface was not determined due to experimental limitations, the actual mechanism behind the observed dealloying phenomena is most certainly owing to the synergy between local heating and the presence of diluted nitric acids.

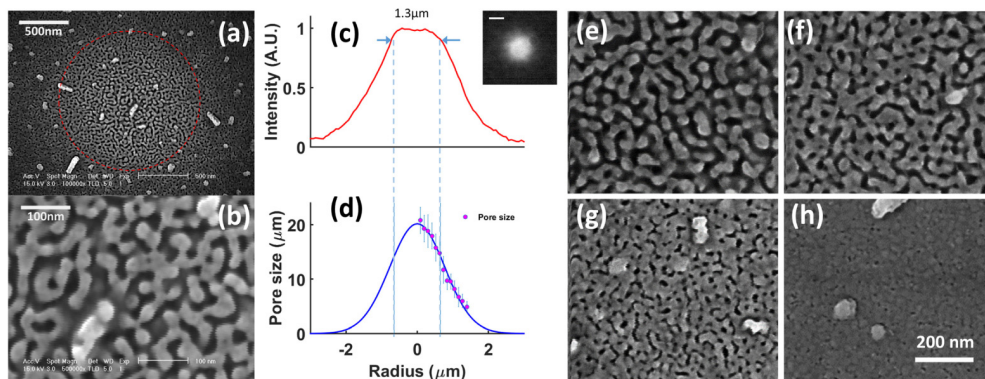


Fig. 2. Characterization of NPG spots: (a) SEM image of an NPG spot. The defined edge of the spot is indicated by a red circle; (b) Zoom-in image at the center of the spot; (c) Cross-sectional view of the bright-field image; inset: bright-field image, scale bar is 2 μm ; (d) Pore size statistics and a Gaussian fit; (e-h) SEM images of different locations from close to far away from the irradiated center. e-h share the same scale bar.

The average NPG spot diameter and the corresponding laser irradiation parameters are summarized in Fig. 3(a). Empty markers indicate bi-continuous pores and ligaments, and solid markers indicate non-continuous structure at the center. In general, longer irradiation time and higher laser power result in larger NPG spots. Below a certain threshold (~ 2 mW), dealloying did not occur within 60 s. The pore size increased with increasing laser power, but was interrupted when the power was higher than 5.6 mW when gas bubbles started to appear. In order to achieve bi-continuous pore and ligament structure as shown in Fig. 2, the temperature should be high enough to elevate the dealloying rate but low enough to prevent the bi-continuous nanoporous structure from coalescing. In particular, for powers higher than 4.9 mW, the bright-field image appears to be in a donut shape. The SEM image of such an NPG spot generated with 4.9 mW for 5 s is shown in Fig. 3(b). The bright-field cross-section profile is shown in Fig. 3(c) in accordance with the red circles indicating the boundaries. The enlarged SEM image of the highlighted area in Fig. 3(b) is shown in Fig. 3(d). Inside the inner boundary of the donut, the ligaments are highly discontinuous with sizes of ~ 50 nm, and the transmission is not as high as the areas with higher connectivity. The larger ligament and pore sizes are due to further diffusion of the Au atoms, while the decrease in transmission could be lower light coupling efficiency due to the change in local plasmonic properties.

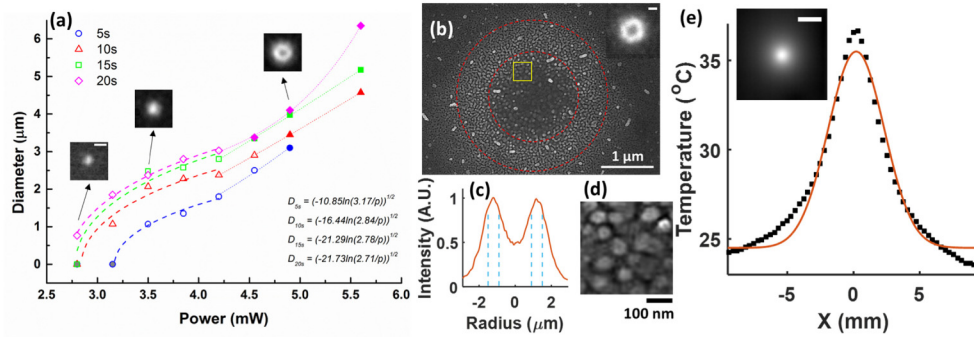


Fig. 3. (a) Different outcomes depending on the laser power and irradiation time of each spot. Gray markers indicate no dealloying, empty markers indicate bi-continuous pores and ligaments, and solid markers indicate non-continuous structure at the center. Insets are bright-field images of NPG spots exposed for 20 s with 2.8, 3.5, and 4.9 mW. Scale bar is 2 μm . (b) Donut-shaped NPG spot. The size threshold is indicated by red circles. The inset is the bright-field image of the spot. Scale bar is 1 μm . (c) Cross-sectional view of the bright-field image. (d) Enlarged SEM image indicated by the yellow square in (b). (e) Center cross-section of the temperature distribution (dotted line) and its Gaussian fit (red curve). Inset: thermal map of the irradiated spot. Scale bar is 5 mm.

As shown in Fig. 2(d), the pore size distribution of an NPG spot can be fitted with a

Gaussian profile. The pore size distribution is described as $d(r) = Te^{-\frac{r^2}{2\sigma^2}}$, where T and α are constants dependent on the specific temperature distribution. We define the diameter $D = 2r$, where r is the distance between the irradiated center and a fixed pore size $d(r) = d_0$, thus $D = 2[-2\sigma^2 \ln(d_0/T)]^{1/2}$. The heat conduction inside a medium irradiated

by a laser beam can be described as $\frac{\partial T(\mathbf{r}, t)}{\partial t} = \alpha \nabla^2 T(\mathbf{r}, t) + \frac{1}{\rho c} Q$, where $\mathbf{r} = (x, y, z)$ is the position, α is the thermal diffusivity, ρ is the medium density, and c is the heat capacity. Using the general solution by Green's function, the temperature at time t' can be written as

$$T(\mathbf{r}, t') = \int_0^{t'} \iiint \frac{Q/\rho c}{(4\pi\alpha t)^{3/2}} e^{-\frac{r^2}{4\alpha t}} dx dy dz dt. \text{ The heat source is } Q = \eta P \text{ where } \eta \text{ is the}$$

photothermal conversion efficiency, laser power $P = P_0 e^{-\frac{r^2}{2\alpha^2}}$, and r_0 is the laser beam radius.

The temperature distribution could be approximated by a Gaussian distribution [27] where the intensity is linear with respect to Q if it is a constant. To further justify this distribution, temperature profile was obtained with a thermal camera (FLIR A320). Due to the resolution limitation of the thermal camera, the temperature profile was acquired with the sample irradiated by a collimated beam of FWHM ~ 1.3 mm from a 532 nm CW laser at 200 mW. Thermal images were acquired from the coverslip side to avoid any inaccuracies caused by high reflectivity of the alloy film. Figure 3(e) shows the center cross-section of the steady-state temperature profile and its Gaussian fit from the temperature distribution map shown in the inset. The mismatch is due to the fact that the Gaussian fit is an approximation of the explicit solution of the temperature distribution. Therefore, the curves in Fig. 3(a) could be fitted with the form of $D = [C_1 \ln(C_2/P)]^{-1/2}$ where C_1 and C_2 are constants. This fitting is no longer valid with powers higher than 4.2 mW. Under the assumption that η is constant, the temperature would reach a plateau and decrease the lateral expansion rate of the dealloying process, in contrary to the diameter-power curves. The inconsistency is caused by

the fact that the photothermal conversion efficiency η is not constant during the dealloying, but a dynamic parameter increased by the forming of plasmonic nanoporous structures. We note that the peak temperature in Fig. 3(e) should not be directly compared to that in the actual dealloying experiment on a microscope because of differences in experimental parameters such as laser power and spot size. In addition, the temperature acquired by the thermal camera is from the backside of the glass coverslip, so the alloy/liquid interface can be considerably hotter. Further, The heat conduction into nitric acid would increase its temperature, but dealloying happens at the interface of alloy and nitric acid, where alloy is the main absorber of incident light. While the heat sinking effect always exists, the temperature of the nitric acid away from the alloy surface plays a lesser role.

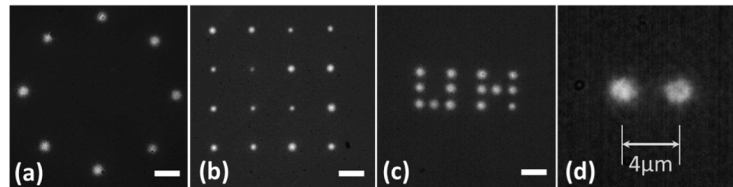


Fig. 4. Bright-field images of dealloyed NPG: (a) 8 points with equal spacing and equal distance ($30\mu\text{m}$) to the center; (b) 4 by 4 grid pattern with $20\mu\text{m}$ inter-spot spacing; (c) “UH” pattern, each letter is $12\mu\text{m} \times 12\mu\text{m}$ in size. a-c share the same scale bar ($10\mu\text{m}$); (d) two adjacent NPG spots $4\mu\text{m}$ apart.

The patterning function has been employed to generate a variety of NPG microstructures. Figure 4 shows the light transmission images of the dealloyed samples using three different laser patterns. The patterns in this work were irradiated in a point-by-point, single-shot process where two consecutive spots were chosen to be far away from each other to avoid excessive heating. The minimum distance between two adjacent spots to be distinguishable is $\sim 4\mu\text{m}$ [Fig. 4d)]. Shorter distance would result in merged NPG spots due to heat accumulation in unirradiated areas, even though the minimum distance did not reach the spatial resolution of our projection system. An alternative method to continuous irradiation is by high-speed scanning ($>250\text{ Hz}$) which can reduce the minimum distance to $\sim 2\mu\text{m}$. In principle, simultaneous patterning of multiple spots is feasible if a more effective heat removal scheme is employed, e.g., by circulating the nearby fluids or employing a substrate with better heat conduction.

Optical characterization of NPG microstructures

Next, we characterize the light transmission of the NPG microstructures. The extinction is calculated as $\log_{10}(I_0/I_t)$ where I_0 and I_t refer to the spectra of the light incident on the sample and the spectrum of light transmitted by the sample, respectively. The extinction spectra of the alloy and NPG microstructure in both air and DI water are shown in Fig. 5(a). The spectra of NPG spots are averaged over the area within the spot boundary. The dotted lines correspond to alloy, and solid lines correspond to NPG spots of diameters 1, 1.2, 1.5 and $1.8\mu\text{m}$. The corresponding SEM images are shown in Fig. 5(b)(i) to (iv), where the left ends of the SEM images indicate the center of the NPG spot. The peak position red-shifted with larger spot size, since the pore sizes inside the boundary are larger with a larger spot size, and the plasmonic resonant peak has a dependence on the pore size [28]. The extinction spectra of alloy are much broader and do not exhibit clearly defined features. In contrast, the extinction spectra of NPG microstructures manifest a well-defined plasmonic peak near 800 nm in the air, and the peak red-shifted in water. Such index-dependent shift was not observed from the alloy film. Among various NPG spots, the largest shift was 36.4 nm , and the corresponding index sensitivity was 110.4 nm/RIU . In addition, the amount of index induced shift increases with NPG spot size. We note that the NPG spots formed by laser-assisted dealloying is

substantially different from sub-wavelength NPG nanoparticles fabricated by lithography as described in our previous works. The laser dealloyed NPG spots have diameters larger than the wavelength of light, are embedded in a continuous alloy film, and have intra-spot pore-size gradient. However, the fact that these NPG spots are larger than the optical wavelength suggests that their optical response would be more similar to continuous NPG thin films, which agrees with our observations.

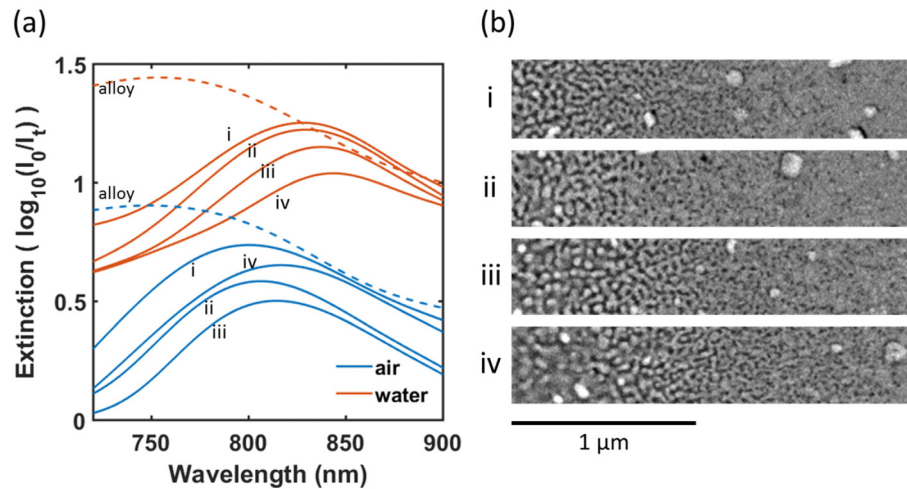


Fig. 5. (a) Extinction spectra of alloy (dotted lines) and NPG spots (solid lines) of different diameters and in different media; (b) SEM images of corresponding NPG spots; Scale bar: 1 μm .

The evolution of nanoporous structure can be monitored using intensity changes in bright-field imaging. There is an average of 6.5 times increase when the NPG microstructures are formed compared to the original alloy film. Therefore, the transmission light intensity can be employed to monitor the formation of NPG microstructures *in situ*. The light transmission intensity can also be an indicator of local refractive index changes. There is a 3.5-fold increase when the environment was changed from air to water. This feature could further contribute to index sensing.

4. Conclusions

We present a novel patterning technique for making nanoporous gold microstructures by generating localized laser heating in diluted nitric acid to selectively dealloy the heated locations. The combination of the heating effect of focused laser and beam patterning via the SLM enable the dealloying process and the patterning process to take place concurrently. The patterned NPG microstructures show gradual changes in pore size and pore connectivity within and around the irradiated area. Parameters including laser power and irradiation duration were investigated with the resulting micro-nanostructures, where the plasmonics effect plays a key role on the material's photothermal light harvesting efficiency as the dealloying proceeds. The patterned NPG microstructures exhibit diameter-dependent red-shift in their extinction spectra. In light transmission measurements, they also exhibit spectral and intensity sensitivity to the local refractive index changes.

Funding

National Science Foundation (NSF) CAREER Awards (CBET-1151154), (CBET-1605683); Gulf of Mexico Research Initiative (GoMRI-030).